

# Polarization sensitive optical coherence tomography of melanin provides intrinsic contrast based on depolarization

Bernhard Baumann,<sup>1,\*</sup> Stefan O. Baumann,<sup>2</sup> Thomas Konegger,<sup>3</sup> Michael Pircher,<sup>1</sup> Erich Götzinger,<sup>1</sup> Ferdinand Schlanitz,<sup>4</sup> Christopher Schütze,<sup>4</sup> Harald Sattmann,<sup>1</sup> Marco Litschauer,<sup>2</sup> Ursula Schmidt-Erfurth,<sup>4</sup> and Christoph K. Hitzenberger<sup>1</sup>

<sup>1</sup>Center for Medical Physics and Biomedical Engineering, Medical University of Vienna, A-1090 Vienna, Austria

<sup>2</sup>Institute of Materials Chemistry, Vienna University of Technology, A-1040 Vienna, Vienna, Austria

<sup>3</sup>Institute of Chemical Technologies and Analytics, Vienna University of Technology, A-1040 Vienna, Austria

<sup>4</sup>Department of Ophthalmology, Medical University and General Hospital of Vienna, A-1090 Vienna, Austria

\*bernhard.baumann@meduniwien.ac.at

**Abstract:** Polarization sensitive optical coherence tomography (PS-OCT) is a functional extension of OCT. In addition to imaging based on tissue reflectivity, PS-OCT also enables depth-resolved mapping of sample polarization properties such as phase-retardation, birefringent axis orientation, Stokes vectors, and degree of polarization uniformity (DOPU). In this study, PS-OCT was used to investigate the polarization properties of melanin. In-vitro measurements in samples with varying melanin concentrations revealed polarization scrambling, i.e. depolarization of backscattered light. Polarization scrambling in the PS-OCT images was more pronounced for higher melanin concentrations and correlated with the concentration of the melanin granules in the phantoms. Moreover, in-vivo PS-OCT was performed in the retinas of normal subjects and individuals with albinism. Unlike in the normal eye, polarization scrambling in the retinal pigment epithelium (RPE) was less pronounced or even not observable in PS-OCT images of albinos. These results indicate that the depolarizing appearance of pigmented structures like, for instance, the RPE is likely to be caused by the melanin granules contained in these cells.

©2012 Optical Society of America

**OCIS codes:** (170.4500) Optical coherence tomography; (230.5440) Polarization-selective devices; (170.6935) Tissue characterization; (170.4580) Optical diagnostics for medicine; (170.4470) Ophthalmology.

## References and links

1. D. Huang, E. A. Swanson, C. P. Lin, J. S. Schuman, W. G. Stinson, W. Chang, M. R. Hee, T. Flotte, K. Gregory, C. A. Puliafito, and J. G. Fujimoto, "Optical coherence tomography," *Science* **254**(5035), 1178–1181 (1991).
2. A. F. Fercher, W. Drexler, C. K. Hitzenberger, and T. Lasser, "Optical coherence tomography-principles and applications," *Rep. Prog. Phys.* **66**(2), 239–303 (2003).
3. J. Walther, M. Gaertner, P. Cimalla, A. Burkhardt, L. Kirsten, S. Meissner, and E. Koch, "Optical coherence tomography in biomedical research," *Anal. Bioanal. Chem.* **400**(9), 2721–2743 (2011).
4. S. Marschall, B. Sander, M. Mogensen, T. M. Jørgensen, and P. E. Andersen, "Optical coherence tomography-current technology and applications in clinical and biomedical research," *Anal. Bioanal. Chem.* **400**(9), 2699–2720 (2011).
5. A. F. Fercher, C. K. Hitzenberger, G. Kamp, and S. Y. Elzaiat, "Measurement of Intraocular Distances by Backscattering Spectral Interferometry," *Opt. Commun.* **117**(1-2), 43–48 (1995).
6. R. Leitgeb, C. K. Hitzenberger, and A. F. Fercher, "Performance of fourier domain vs. time domain optical coherence tomography," *Opt. Express* **11**(8), 889–894 (2003).
7. J. F. de Boer, B. Cense, B. H. Park, M. C. Pierce, G. J. Tearney, and B. E. Bouma, "Improved signal-to-noise ratio in spectral-domain compared with time-domain optical coherence tomography," *Opt. Lett.* **28**(21), 2067–2069 (2003).
8. M. A. Choma, M. V. Sarunic, C. H. Yang, and J. A. Izatt, "Sensitivity advantage of swept source and Fourier domain optical coherence tomography," *Opt. Express* **11**(18), 2183–2189 (2003).
9. W. Drexler and J. G. Fujimoto, "State-of-the-art retinal optical coherence tomography," *Prog. Retin. Eye Res.* **27**(1), 45–88 (2008).

10. M. R. Hee, D. Huang, E. A. Swanson, and J. G. Fujimoto, "Polarization-sensitive low-coherence reflectometer for birefringence characterization and ranging," *J. Opt. Soc. Am. B* **9**(6), 903–908 (1992).
11. J. F. de Boer, T. E. Milner, and J. S. Nelson, "Determination of the depth-resolved Stokes parameters of light backscattered from turbid media by use of polarization-sensitive optical coherence tomography," *Opt. Lett.* **24**(5), 300–302 (1999).
12. B. Cense, T. C. Chen, B. H. Park, M. C. Pierce, and J. F. de Boer, "Thickness and birefringence of healthy retinal nerve fiber layer tissue measured with polarization-sensitive optical coherence tomography," *Invest. Ophthalmol. Vis. Sci.* **45**(8), 2606–2612 (2004).
13. C. K. Hitzenberger, E. Goetzinger, M. Sticker, M. Pircher, and A. F. Fercher, "Measurement and imaging of birefringence and optic axis orientation by phase resolved polarization sensitive optical coherence tomography," *Opt. Express* **9**(13), 780–790 (2001).
14. E. Götzinger, M. Pircher, W. Geitzenauer, C. Ahlers, B. Baumann, S. Michels, U. Schmidt-Erfurth, and C. K. Hitzenberger, "Retinal pigment epithelium segmentation by polarization sensitive optical coherence tomography," *Opt. Express* **16**(21), 16410–16422 (2008).
15. S. Jiao and L. V. Wang, "Jones-matrix imaging of biological tissues with quadruple-channel optical coherence tomography," *J. Biomed. Opt.* **7**(3), 350–358 (2002).
16. S. Jiao and L. V. Wang, "Two-dimensional depth-resolved Mueller matrix of biological tissue measured with double-beam polarization-sensitive optical coherence tomography," *Opt. Lett.* **27**(2), 101–103 (2002).
17. B. H. Park, M. C. Pierce, B. Cense, and J. F. de Boer, "Jones matrix analysis for a polarization-sensitive optical coherence tomography system using fiber-optic components," *Opt. Lett.* **29**(21), 2512–2514 (2004).
18. M. Miura, M. Yamanari, T. Iwasaki, A. E. Elsner, S. Makita, T. Yatagai, and Y. Yasuno, "Imaging polarimetry in age-related macular degeneration," *Invest. Ophthalmol. Vis. Sci.* **49**(6), 2661–2667 (2008).
19. S. Michels, M. Pircher, W. Geitzenauer, C. Simader, E. Götzinger, O. Findl, U. Schmidt-Erfurth, and C. K. Hitzenberger, "Value of polarisation-sensitive optical coherence tomography in diseases affecting the retinal pigment epithelium," *Br. J. Ophthalmol.* **92**(2), 204–209 (2008).
20. M. Pircher, E. Götzinger, R. Leitgeb, H. Sattmann, O. Findl, and C. Hitzenberger, "Imaging of polarization properties of human retina in vivo with phase resolved transversal PS-OCT," *Opt. Express* **12**(24), 5940–5951 (2004).
21. M. Yamanari, S. Makita, and Y. Yasuno, "Polarization-sensitive swept-source optical coherence tomography with continuous source polarization modulation," *Opt. Express* **16**(8), 5892–5906 (2008).
22. M. Pircher, C. K. Hitzenberger, and U. Schmidt-Erfurth, "Polarization sensitive optical coherence tomography in the human eye," *Prog. Retin. Eye Res.* **30**(6), 431–451 (2011).
23. M. Pircher, E. Goetzinger, R. Leitgeb, and C. K. Hitzenberger, "Transversal phase resolved polarization sensitive optical coherence tomography," *Phys. Med. Biol.* **49**(7), 1257–1263 (2004).
24. C. Ahlers, E. Götzinger, M. Pircher, I. Golbaz, F. Prager, C. Schütze, B. Baumann, C. K. Hitzenberger, and U. Schmidt-Erfurth, "Imaging of the retinal pigment epithelium in age-related macular degeneration using polarization-sensitive optical coherence tomography," *Invest. Ophthalmol. Vis. Sci.* **51**(4), 2149–2157 (2010).
25. B. Baumann, E. Götzinger, M. Pircher, H. Sattmann, C. Schütze, F. Schlanitz, C. Ahlers, U. Schmidt-Erfurth, and C. K. Hitzenberger, "Segmentation and quantification of retinal lesions in age-related macular degeneration using polarization-sensitive optical coherence tomography," *J. Biomed. Opt.* **15**(6), 061704 (2010).
26. B. Baumann, E. Götzinger, M. Pircher, and C. K. Hitzenberger, "Measurements of depolarization distribution in the healthy human macula by polarization sensitive OCT," *J Biophotonics* **2**(6-7), 426–434 (2009).
27. L. Feeney-Burns, E. S. Hilderbrand, and S. Eldridge, "Aging human RPE: morphometric analysis of macular, equatorial, and peripheral cells," *Invest. Ophthalmol. Vis. Sci.* **25**(2), 195–200 (1984).
28. J. J. Weiter, F. C. Delori, G. L. Wing, and K. A. Fitch, "Retinal pigment epithelial lipofuscin and melanin and choroidal melanin in human eyes," *Invest. Ophthalmol. Vis. Sci.* **27**(2), 145–152 (1986).
29. C. N. Keilhauer and F. C. Delori, "Near-infrared autofluorescence imaging of the fundus: visualization of ocular melanin," *Invest. Ophthalmol. Vis. Sci.* **47**(8), 3556–3564 (2006).
30. B. Baumann, S. O. Baumann, T. Konegger, M. Pircher, E. Goetzinger, H. Sattmann, M. Litschauer, and C. K. Hitzenberger, "Polarization sensitive optical coherence tomography of melanin provides tissue inherent contrast based on depolarization," *Proc. SPIE* **7554**, 75541M, 75541M-6 (2010).
31. P. Giacomoni, L. Marrot, M. Mellul, and A. Colette, "Process for the preparation of a small size melanic pigment and its use in cosmetics," PCT Patent 1994/025531 (1994).
32. K. M. Zinn and J. V. Benjamin-Henkind, "Anatomy of the human retinal pigment epithelium," in *The Retinal Pigment Epithelium*, K. M. Zinn and M. F. Marmor, eds. (Harvard University Press, 1979).
33. American national standard for safe use of lasers. ANSI Z 136.1 (Laser Institute of America, 2000).
34. International Electrotechnical Commission, Safety of laser products - Part 1: Equipment classification and requirements, IEC 60825–1 Ed. 2 (IEC, 2001).
35. E. Götzinger, M. Pircher, and C. K. Hitzenberger, "High speed spectral domain polarization sensitive optical coherence tomography of the human retina," *Opt. Express* **13**(25), 10217–10229 (2005).
36. M. Wojtkowski, V. J. Srinivasan, T. H. Ko, J. G. Fujimoto, A. Kowalczyk, and J. S. Duker, "Ultrahigh-resolution, high-speed, Fourier domain optical coherence tomography and methods for dispersion compensation," *Opt. Express* **12**(11), 2404–2422 (2004).
37. J. F. de Boer, T. E. Milner, M. J. C. van Gemert, and J. S. Nelson, "Two-dimensional birefringence imaging in biological tissue by polarization-sensitive optical coherence tomography," *Opt. Lett.* **22**(12), 934–936 (1997).
38. M. J. Everett, K. Schoenberger, B. W. Colston, Jr., and L. B. Da Silva, "Birefringence characterization of biological tissue by use of optical coherence tomography," *Opt. Lett.* **23**(3), 228–230 (1998).

39. M. Pircher, E. Götzinger, O. Findl, S. Michels, W. Geitzenauer, C. Leydolt, U. Schmidt-Erfurth, and C. K. Hitzenberger, "Human macula investigated in vivo with polarization-sensitive optical coherence tomography," *Invest. Ophthalmol. Vis. Sci.* **47**(12), 5487–5494 (2006).
40. J. M. Schmitt and S. H. Xiang, "Cross-polarized backscatter in optical coherence tomography of biological tissue," *Opt. Lett.* **23**(13), 1060–1062 (1998).
41. J. F. de Boer and T. E. Milner, "Review of polarization sensitive optical coherence tomography and Stokes vector determination," *J. Biomed. Opt.* **7**(3), 359–371 (2002).
42. M. I. Mishchenko and J. W. Hovenier, "Depolarization of light backscattered by randomly oriented nonspherical particles," *Opt. Lett.* **20**(12), 1356–1358 (1995).
43. M. Ahmad, S. Alali, A. Kim, M. F. G. Wood, M. Ikram, and I. A. Vitkin, "Do different turbid media with matched bulk optical properties also exhibit similar polarization properties?" *Biomed. Opt. Express* **2**(12), 3248–3258 (2011).
44. E. Götzinger, M. Pircher, B. Baumann, C. Ahlers, W. Geitzenauer, U. Schmidt-Erfurth, and C. K. Hitzenberger, "Three-dimensional polarization sensitive OCT imaging and interactive display of the human retina," *Opt. Express* **17**(5), 4151–4165 (2009).
45. R. E. Carr and I. M. Siegel, "The Retinal Pigment Epithelium in Ocular Albinism," in *The Retinal Pigment Epithelium*, K. M. Zinn and M. F. Marmor, eds. (Harvard University Press, 1979).
46. G. T. Chong, S. Farsiu, S. F. Freedman, N. Sarin, A. F. Koreishi, J. A. Izatt, and C. A. Toth, "Abnormal foveal morphology in ocular albinism imaged with spectral-domain optical coherence tomography," *Arch. Ophthalmol.* **127**(1), 37–44 (2009).
47. J. T. McAllister, A. M. Dubis, D. M. Tait, S. Ostler, J. Rha, K. E. Stepien, C. G. Summers, and J. Carroll, "Arrested development: high-resolution imaging of foveal morphology in albinism," *Vision Res.* **50**(8), 810–817 (2010).
48. B. Cense, N. Nassif, T. C. Chen, M. C. Pierce, S. H. Yun, B. H. Park, B. Bouma, G. Tearney, and J. F. de Boer, "Ultrahigh-resolution high-speed retinal imaging using spectral-domain optical coherence tomography," *Opt. Express* **12**(11), 2435–2447 (2004).
49. V. J. Srinivasan, B. K. Monson, M. Wojtkowski, R. A. Bilonick, I. Gorczynska, R. Chen, J. S. Duker, J. S. Schuman, and J. G. Fujimoto, "Characterization of outer retinal morphology with high-speed, ultrahigh-resolution optical coherence tomography," *Invest. Ophthalmol. Vis. Sci.* **49**(4), 1571–1579 (2008).
50. A. L. Kornzweig, "Aging of the retinal pigment epithelium," in *The Retinal Pigment Epithelium*, K. M. Zinn and M. F. Marmor, eds. (Harvard University Press, 1979).
51. U. Schraermeyer and K. Heimann, "Current understanding on the role of retinal pigment epithelium and its pigmentation," *Pigment Cell Res.* **12**(4), 219–236 (1999).
52. S. Schmitz-Valckenberg, D. Lara, S. Nizari, E. M. Normando, L. Guo, A. R. Wegener, A. Tufail, F. W. Fitzke, F. G. Holz, and M. F. Cordeiro, "Localisation and significance of in vivo near-infrared autofluorescent signal in retinal imaging," *Br. J. Ophthalmol.* **95**(8), 1134–1139 (2011).
53. X. Zhang, H. F. Zhang, C. A. Puliafito, and S. Jiao, "Simultaneous in vivo imaging of melanin and lipofuscin in the retina with photoacoustic ophthalmoscopy and autofluorescence imaging," *J. Biomed. Opt.* **16**(8), 080504 (2011).
54. H. Miettinen, W. R. Green, S. M. Wolff, and G. P. Abundo, "Foveal hypoplasia in complete oculocutaneous albinism. A histopathologic study," *Retina* **12**(3), 254–260 (1992).
55. B. Baumann, W. Choi, B. Potsaid, D. Huang, J. S. Duker, and J. G. Fujimoto, "Swept source/Fourier domain polarization sensitive optical coherence tomography with a passive polarization delay unit," *Opt. Express* **20**(9), 10218–10230 (2012).
56. M. Pircher, E. Götzinger, R. Leitgeb, and C. K. Hitzenberger, "Three dimensional polarization sensitive OCT of human skin in vivo," *Opt. Express* **12**(14), 3236–3244 (2004).
57. S. L. Jiao, M. S. Jiang, J. M. Hu, A. Fawzi, Q. F. Zhou, K. K. Shung, C. A. Puliafito, and H. F. Zhang, "Photoacoustic ophthalmoscopy for in vivo retinal imaging," *Opt. Express* **18**(4), 3967–3972 (2010).

---

## 1. Introduction

Ever since its first presentation in 1991, optical coherence tomography (OCT) has found applications in manifold fields [1]. Its ability to perform non-invasive, non-contact imaging of weakly scattering structures with micrometer-scale resolution in real time has made OCT particularly attractive for investigating biological tissues in vivo [2–4]. The recent development of OCT techniques using Fourier domain detection has led to an immense increase of detection sensitivity which allowed for recording three-dimensional (3D) OCT data sets within a few seconds [5–8]. Consequently, OCT has been applied for volumetric high-resolution imaging in biomedical fields such as endoscopic investigations of the gastrointestinal tract or intravascular probing. The most prominent application of OCT, however, is in ophthalmology where it has become an essential tool in everyday clinical routine. OCT's ability to resolve single retinal layers has been used for diagnosis of pathology, monitoring disease progression and follow-up imaging of response to therapy [9].

Current developments of OCT technology pursue further improvement of image resolution, increasing imaging speeds and finding new ways to enhance image contrast.

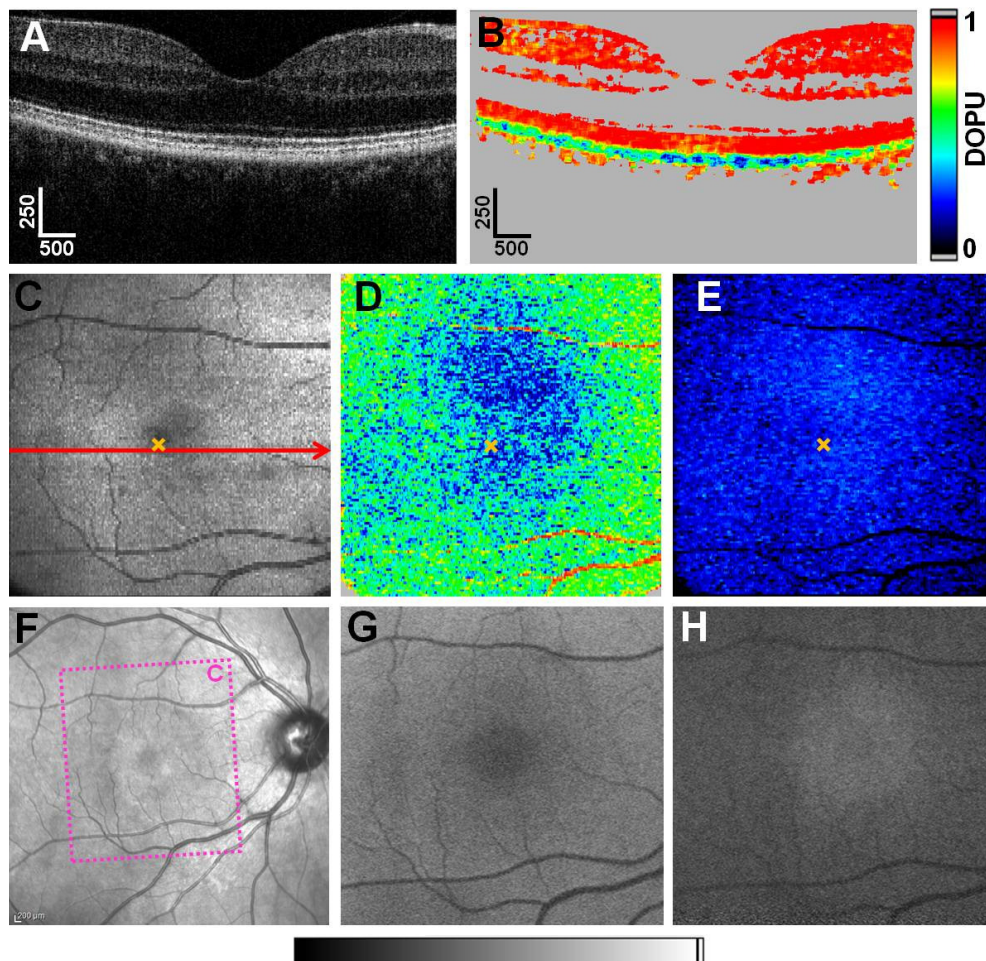


Fig. 1. PS-OCT imaging and retinal pigmentation. (A) Reflectivity B-scan image showing the retinal layers. (B) Corresponding degree of polarization uniformity (DOPU) B-scan image. DOPU values close to 1 can be observed in most retinal layers. Lower DOPU values indicate depolarization and can be observed in the pigmented RPE and choroid. See section 2.3 for a detailed description of DOPU calculations. (C) OCT fundus projection image of a volumetric PS-OCT data set of the macula. The red arrow indicates the location of the B-scan image shown in (A). The orange “x” marks the fovea in (C-E). (D)  $DOPU_{min}$  map showing the minimal DOPU value for every A-scan. The color scale encodes  $DOPU_{min}$  values ranging from 0 (blue) to 1 (red). The most severe depolarization can be observed close to the fovea. (E) Thickness map of segmented depolarizing pixels with  $DOPU < 0.7$ . The color scale ranges from 0 to 39 pixels per A-line. Pixel height:  $3.22 \mu\text{m}$  in air. (F) Wide-field infrared scanning laser ophthalmoscope image. The dotted box indicates the location of the PS-OCT scan. (G) Corresponding fundus autofluorescence image at 488 nm showing the retinal lipofuscin distribution having a minimum at the fovea. (H) Near-infrared autofluorescence image at 787 nm showing the retinal melanin distribution peaking at the fovea. Grey scale bar for the scanning laser ophthalmoscope image and the autofluorescence images is shown below (F-H). Scale bar dimensions in micrometers.

Polarization sensitive (PS) optical coherence tomography is often referred to as a “functional” extension of OCT and provides depth-resolved imaging of the polarization properties of sample structures [10]. Other than standard, intensity-based OCT, which provides image contrast based on the amount of light backscattered from different sites inside

the sample, PS-OCT opens access to an additional contrast channel: By illuminating the sample with light in a well-defined polarization state and by using a polarization sensitive detection unit, not only reflectivity but also the polarization state of light can be assessed three-dimensionally. From the detected polarization state, phase retardation, optic axis orientation as well as Stokes vectors can be calculated [10–13]. PS-OCT has also been demonstrated for 3D assessment of depolarization and diattenuation as well as for imaging of complete Jones matrices and Müller matrices [14–17].

In the human eye, PS-OCT imaging allows one to distinguish structures with birefringent (e.g., corneal stroma, retinal nerve fiber layer), polarization preserving (e.g., stroma of the iris, photoreceptor layer), and depolarizing (e.g., pigment epithelia of iris and retina) properties [12,18–23]. It was shown that the polarization-scrambling, i.e. depolarizing, characteristics of the retinal pigment epithelium (RPE) can be used for segmenting that layer [14]. In diseased retinas, this enables it to assess retinal disorders – such as drusen areas and volumes as well as the areas of atrophic zones in age-related macular degeneration (AMD) – in a quantitative way [24,25].

Recently, we investigated the depolarizing character of the RPE in the macula region of healthy volunteers [26]. An example for macular PS-OCT imaging is shown in Fig. 1. The RPE's depolarization appeared most pronounced close to the center of the fovea and decreased in the periphery (Fig. 1(B) and (D)). However, the origin of the polarization scrambling is still unclear and could be caused by the outer morphology of the RPE cells or by their structural composition. In addition to regular cell organelles like mitochondria or cell nuclei, the human RPE cells contain different pigments in granular shape: melanin, lipofuscin, and composites of both [27]. While the lipofuscin concentration has a minimum in the fovea and increases in the periphery of the posterior pole (Fig. 1(G)), the concentration of melanin shows the inverse characteristic with a peak concentration in the fovea (Fig. 1(H)) [27–29]. Since the macular distribution of melanin appears congruent with the depolarization pattern measured with PS-OCT [26], this implies that melanin could be the origin of the RPE's polarization scrambling property. In order to verify this hypothesis, measurements in phantoms are necessary.

In this paper, we present a melanin granule model to investigate the origin of polarization scrambling in PS-OCT images (based on [30]). In addition to results from measurements in these pigment phantoms, we demonstrate 3D PS-OCT imaging of retinas with regular pigmentation and – for the first time – ocular albinism featuring irregular pigmentation.

## 2. Methods

### 2.1 Melanin phantoms

Melanin models of different concentrations were generated to simulate the effect of RPE pigmentation. From raw eumelanin (Sigma Aldrich), ellipsoidal melanin particles were produced by dissolving in a sodium carbonate solution and re-precipitating upon addition of calcium chloride [31]. A narrow size distribution of the melanin particles with a maximum at ~530 nm was observed by dynamic light scattering (DLS) measurements which were performed with an ALV/CGS-3 compact goniometer system with an ALV/LSE-5003 light scattering electronics and multiple  $\tau$  digital correlator at 25 °C (Fig. 2(D)). This size corresponds well to the dimension of melanin granules in the human RPE cells reported in literature [32] (Fig. 2(F)). Scanning electron micrographs of the powder, which were recorded on a FEI Quanta 200 Mk2, revealed particles in the respective sizes and shapes (cf. Fig. 2(A)–2(C)).

Using distilled water, dispersions with melanin volume concentrations  $C_{\text{mel}} = V_{\text{mel}} \cdot V_{\text{water}}$  in the range from 1:1 to 1:100 were prepared. The suspensions were treated with ultrasound for 30 seconds in order to break up particle agglomerates and to prevent the formation thereof.

## 2.2 PS-OCT system

PS-OCT imaging of both melanin phantoms and human retinas was performed using our recently reported clinical PS-OCT instrument [25]. In brief, the system design is based on a free-space Michelson interferometer with additional polarization optics. A broadband superluminescent diode (Superlum Diodes, Inc.) centered at 839 nm with an FWHM bandwidth of 58 nm was employed as a light source. Circularly polarized light was used to illuminate the sample. The sample arm power of  $\sim 700 \mu\text{W}$  was well below the safety limits for retinal imaging given by ANSI and IEC [33,34]. At the interferometer exit, the OCT signal was split into two orthogonal polarization components, which were simultaneously detected by two identical spectrometer units. Every readout of the spectrometer line scan cameras yielded the spectral data necessary to compute not only depth-resolved reflectivity, but also phase retardation, optic axis orientation and Stokes vectors for one depth profile [35]. Operating at an A-line rate of 20 kHz, the system sensitivity was  $\sim 98 \text{ dB}$  for each polarization channel.

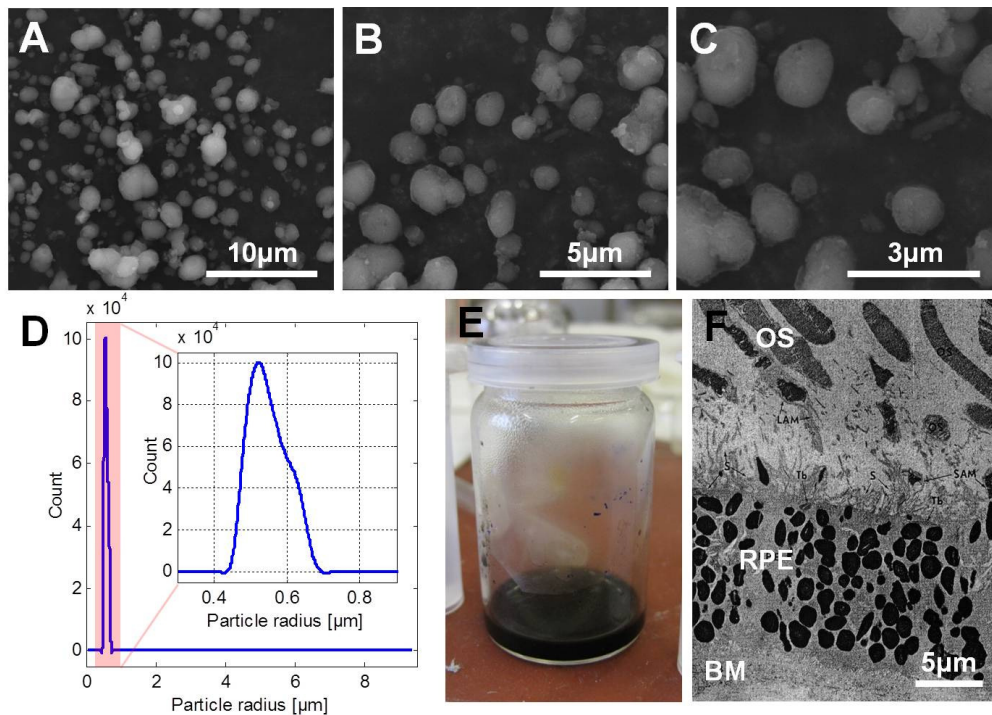


Fig. 2. Melanin granule samples. (A-C) Scanning electron micrographs of the melanin granules at different magnifications. (D) Size distribution measured with DLS. A narrow size distribution centered at a particle radius of  $\sim 530 \text{ nm}$  was measured. (E) Melanin suspension. (F) Transmission electron micrograph of the retina at the level of the RPE. Acronyms: BM Bruch's membrane, OS outer segment. (Image reprinted from ref [32]. with permission from Prof. Michael F. Marmor from the Department of Ophthalmology, Stanford University School of Medicine).

The PS-OCT system includes an additional detection channel, which allows it to record scanning laser ophthalmoscope (SLO) images by detecting the horizontally polarized light portion of light returning from the sample into the source arm. The PS-OCT and SLO subsystems share the same light source and sample arm optics. Controlled by a field programmable gate array (FPGA), the system can record and display OCT and SLO images in an alternate fashion, which allows for real-time monitoring of the retinal position during alignment of the eye under investigation.

Using this PS-OCT system, 3D data sets ( $1024 \times 64 \times 1024$  voxels,  $12 \times 12 \times 3.3$  mm<sup>3</sup>, orientation:  $x \times y \times z$ ) of melanin suspensions were recorded. The liquid suspensions were imaged inside of a cylindrical glass container immediately after ultrasonification (Fig. 2(E)). The samples were imaged in 3D in order to be insensitive to container alignment in  $x$ - and  $y$ -direction. Evaluation of a PS-OCT data set recorded in the empty container confirmed the polarization preserving characteristics of the container material.

For retinal imaging, 3D data sets of both  $1024 \times 64 \times 1024$  and  $512 \times 128 \times 1024$  voxels ( $6.2 \times 6.7 \times 3.3$  mm<sup>3</sup>) were recorded using the PS-OCT instrument. Healthy subjects as well as albino patients were imaged. The study protocol adhered to the tenets of the declaration of Helsinki and was approved by the ethics committee of the Medical University of Vienna. Written informed consent was obtained from each subject prior to the study.

### 2.3 Quantification of depolarization – degree of polarization uniformity

In order to assess polarization scrambling in PS-OCT images, a quantity called degree of polarization uniformity (DOPU) was used. For each B-scan, the spectral signals recorded at the two exits of the PS-OCT instrument were processed using regular SD-OCT processing including background subtraction, remapping to equidistant sampling in  $k$ -space, numerical dispersion compensation, and Fourier transformation [36]. The Stokes vector elements ( $I, Q, U, V$ )<sup>T</sup> were calculated from the amplitudes and phases of the two polarization channels' OCT signals for each image pixel. The first Stokes vector element  $I$  (corresponding to backscattered intensity) was used to identify pixels with low intensity, which consequently were excluded from further calculation. The Stokes vector elements of the remaining pixels were then normalized and averaged in a sliding evaluation window yielding  $Q_{\text{mean}}(x,y,z)$ ,  $U_{\text{mean}}(x,y,z)$ , and  $V_{\text{mean}}(x,y,z)$ . The degree of polarization uniformity, DOPU, was then computed as [14]

$$DOPU = \sqrt{Q_{\text{mean}}^2 + U_{\text{mean}}^2 + V_{\text{mean}}^2} . \quad (1)$$

DOPU has a form similar to that of the degree of polarization (DOP) known from polarization optics. However, since PS-OCT relies on coherent detection of light, DOP will always read  $DOP = \sqrt{Q'^2 + U'^2 + V'^2} = 1$ , where the prime indicates normalization of one pixel's Stokes vector elements by  $I$ . In contrast, DOPU results from an average of the Stokes vector elements of different speckles and, therefore, provides a measure for the uniformity of the polarization states within the evaluation window. In order to enable both coverage of enough speckles for statistics and decent spatial resolution in the DOPU images, evaluation window sizes of  $100(x) \times 16(z)$   $\mu\text{m}^2$  (i.e.,  $8(x) \times 5(z)$  and  $16(x) \times 5(z)$  pixels, respectively) were chosen. For polarization preserving and birefringent structures, DOPU values close to 1 will be observed, whereas polarization scrambling will result in lower DOPU values.

## 3. Results

### 3.1 Melanin phantoms

PS-OCT imaging was performed in melanin suspensions with 13 different volume concentrations ranging from  $C_{\text{mel}} = 0.01$  to  $C_{\text{mel}} = 1$ . Figures 3(A) and (B) show reflectivity B-scan images of the suspensions with  $C_{\text{mel}} = 1:60$  and  $C_{\text{mel}} = 1:3$ , respectively. The corresponding DOPU B-scan images are shown in Figs. 3(C) and (D). The DOPU images are color coded from blue (DOPU = 0) to red (DOPU = 1). Pixels with intensities below a threshold set to  $\sim 3.5$  standard deviations of the noise intensity above the mean noise level are displayed in grey. While the reflectivity images exhibit rather similar appearance, obvious changes can be observed in the DOPU images for different  $C_{\text{mel}}$ . In order to evaluate the depolarization characteristics of the melanin suspension, the average DOPU was computed for the different concentrations  $C_{\text{mel}}$  in an area of  $5.86(x) \times 0.84(z)$  mm<sup>2</sup> ( $500(x) \times 260(z)$  pixels).

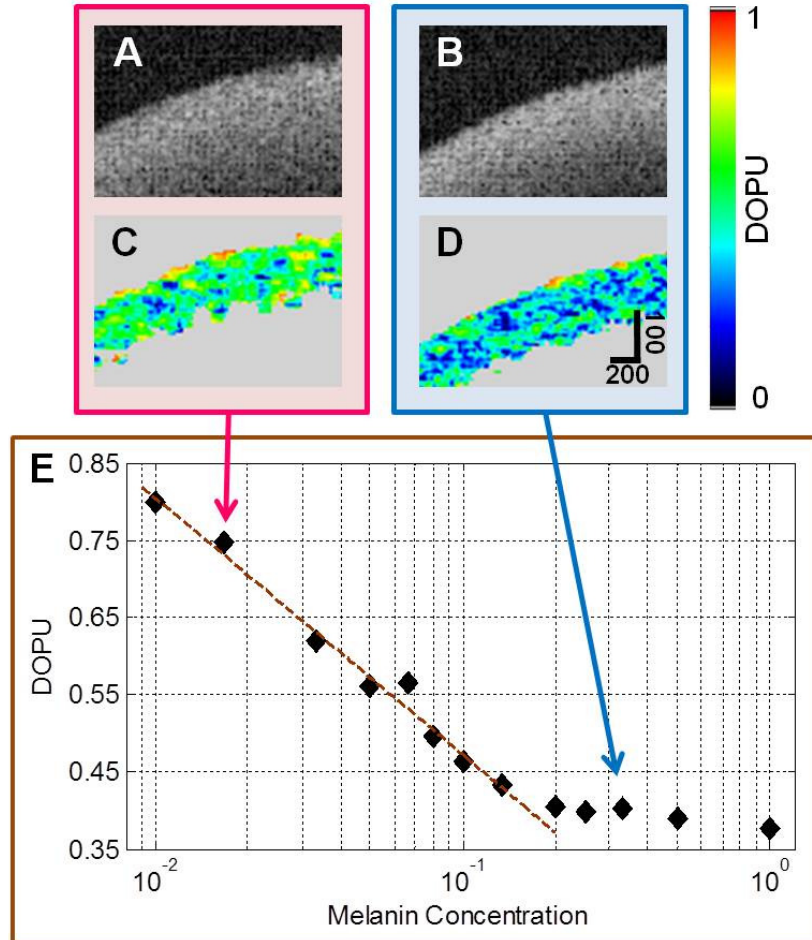


Fig. 3. PS-OCT measurements of melanin samples. (A, B) Reflectivity B-scan images for melanin concentrations  $C_{mel}$  of 1:60 and 1:3, respectively. (C, D) Corresponding DOPU images showing increasing average DOPU for decreasing melanin concentration. Scale bars dimensions in micrometers. (E) DOPU vs. melanin concentration. For melanin suspensions ranging from 1:100 to 1:1, average DOPU values measured within the melanin suspensions are plotted. A trend from high to low DOPU values can be observed when the concentration is increasing. The dashed brown line is a logarithmic fit to the data:  $DOPU = B \cdot \ln(C_{mel}) - A$ , where  $A = -0.1408$  and  $B = -0.144$ .

For high melanin concentrations,  $C_{mel} = 1:1$  to  $1:5$ , DOPU values are rather constant at  $0.39 \pm 0.01$ . These low DOPU values indicate strong polarization scrambling, i.e. the highly depolarizing characteristic of the suspension with high melanin concentration. Starting from  $C_{mel} = 1:7.5$ , a monotonic increase of DOPU values can be observed as  $C_{mel}$  decreases. At low melanin concentrations, high DOPU values indicate less depolarization in the phantoms.

### 3.2 Depolarization imaging in the normal and albino human retina

In the previous section, we demonstrated the dependence of depolarization in PS-OCT images on the pigment concentration in melanin phantoms. Next, we show examples of PS-OCT images in human subjects with different retinal pigmentation.

Retinal PS-OCT images of a normal subject are shown in Fig. 4. In the reflectivity B-scan image, the retinal layers appear as known from standard OCT (Fig. 4(A)). Figure 4(D) shows details of the outer retinal layers: The layers associated with the photoreceptors – i.e., the external limiting membrane (ELM), the junction of the inner and outer photoreceptor

segments (IS/OS), and the end tips of the photoreceptors (ETPR) – can be observed as thin, hyperreflective lines. Posterior to the photoreceptors, the RPE appears as a diffuse, hyperreflective layer. In the corresponding phase retardation images, rather constant values can be observed in the polarization preserving outer retinal layers (Figs. 4(B) and 4(E)). In contrast, the RPE exhibits strongly varying retardation values, which manifest in a dotted appearance with pixel colors ranging from blue over green to orange. This polarization scrambling characteristic of the RPE is also obvious in the DOPU images (Figs. 4(C) and 4(F)). While most retinal layers exhibit DOPU values close to 1, indicating rather uniform polarization, depolarization in the RPE manifests in lower DOPU values.

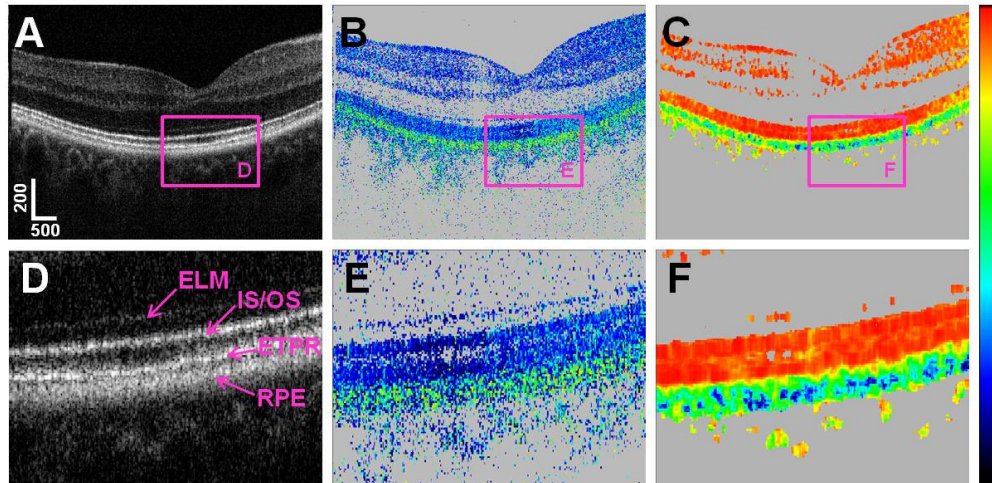


Fig. 4. Retinal PS-OCT imaging in a normal subject. (A) Reflectivity B-scan image of the fovea region. (B) Corresponding phase retardation B-scan image (color scale:  $0^\circ - 90^\circ$ ). (C) DOPU image (color scale: 0 – 1). (D–F) Details of (A), (B), and (C), respectively. While the photoreceptor interfaces can be observed as thin layers in (A) and (D), the RPE exhibits a fuzzy appearance. In the phase retardation images (B) and (E), polarization scrambling can be observed in the RPE as blue, green, and even orange dots. Accordingly, the RPE exhibits low values in the DOPU images (C) and (F). The inner retinal layers present rather uniform polarization characteristics and hence DOPU values close to 1. Scale bar dimensions in micrometers.

PS-OCT imaging was also performed in the eyes of two subjects with ocular albinism of different stages of lack of pigmentation. However, obvious differences in the appearance of the RPE can already be observed in albino patient 1 presenting with mild depigmentation. While apart from the obvious foveal hypoplasia, the inner retinal layers look similar to the corresponding layers in normal subjects, obvious differences can be observed in the RPE/BM complex in the reflectivity B-scan images (Figs. 5(A) and 5(D)): The previously fuzzy hyperreflective structure now appears as two tightly spaced thin lines. Further, polarization scrambling is less obvious in the phase retardation images (Figs. 5(B) and 5(E)). This translates into unusual, high DOPU values in the RPE, and thus into a more uniform shading of all retinal layers including the RPE (Figs. 5(C) and 5(F)).

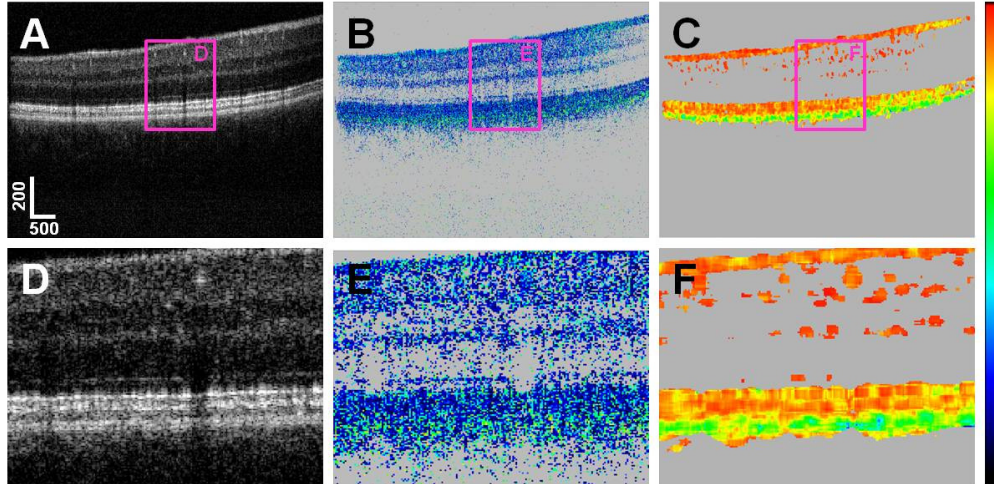


Fig. 5. PS-OCT imaging in the retina of albino patient 1. (A, D) Reflectivity B-scan images. The RPE/BM complex showing two distinct layers. (B, E) Corresponding phase retardation images. Compared to the normal retina in Fig. 4, there is less polarization scrambling in the RPE. (C, F) DOPU images. In comparison to the respective images in Fig. 4, the DOPU values in the polarization scrambling layer indicate less depolarization. Scale bar dimensions in micrometers.

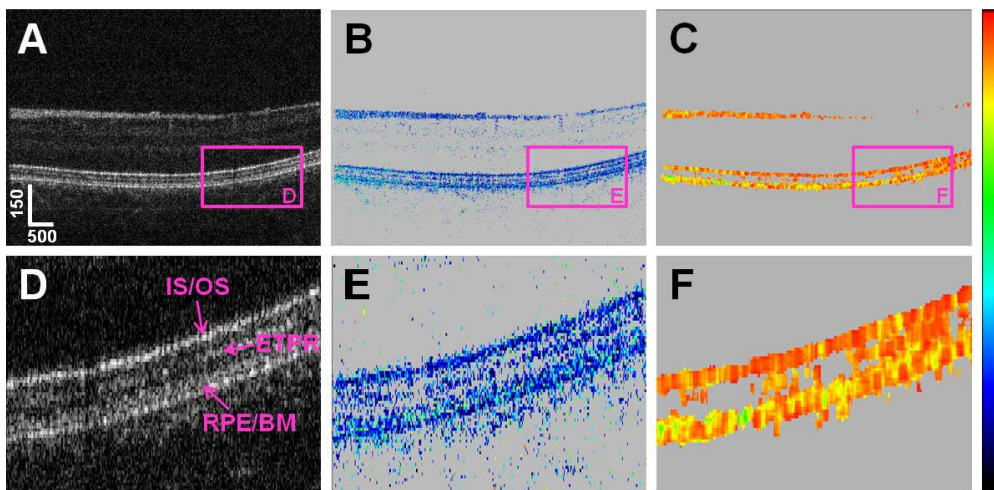


Fig. 6. PS-OCT imaging in the retina of albino patient 2. (A, D) Reflectivity B-scan images. At the level of the RPE/BM complex, the BM stands out as a thin hyperreflective line, while the RPE is less visible. (B, E) Corresponding phase retardation images. The RPE/BM complex completely lacks its polarization scrambling characteristic. It appears blue, just like the polarization preserving photoreceptor layer. (C, F) DOPU images. In agreement with the bluish appearance of the RPE/BM complex in the phase retardation image, rather uniform polarization, i.e. high DOPU values, can be observed in this structure. Both the usually polarization scrambling RPE and the inner retinal layers have a similar, orange/reddish shade. Scale bar dimensions in micrometers.

Even more pronounced differences are apparent in another albino patient (Fig. 6). While also in this patient the RPE/BM structures can be observed as clearly separated lines rather than one diffuse layer (Figs. 6(A) and 6(D)), their different appearance in the PS-OCT images is evident at first glance: Neither in the phase retardation images (Figs. 6(B) and 6(E)) nor in the DOPU images (Figs. 6(C) and 6(F)), the specific depolarization contrast can be observed in the RPE. Looking at this albino patient's RPE in the retardation and DOPU images, the

RPE appears rather blue and reddish, respectively – just like the polarization preserving photoreceptors.

#### 4. Discussion

PS-OCT has emerged as a functional extension of OCT. Imaging the sample's polarization properties has enabled additional image contrast and quantitative measurements. While tissue birefringence had already been a subject of investigations in early reports on PS-OCT [10,37,38], polarization scrambling in PS-OCT has been discovered and investigated only recently [20,26,39]. In the human eye, depolarization was found in the pigment epithelia of the retina and iris, as well as in the choroid. Depolarization in the RPE was used as a tissue specific contrast and further as a useful tissue property for segmentation of this layer [14]. The distribution of the depolarizing appearance of the RPE was found to be congruent with the distribution of the melanin granules [26]. As a logical consequence to these findings, we performed PS-OCT measurements in melanin phantoms in order to investigate the polarization properties of isolated melanin granules in various concentrations.

The results detailed in section 3.1 showed a strong correlation between melanin granule concentration and polarization scrambling. For high melanin concentrations in the phantoms, depolarization manifested in low DOPU values, saturating with a plateau at melanin concentrations  $C_{mel} \geq 0.2$ . For lower concentrations of the ellipsoidal melanin particles in the water suspension, an exponential relationship between  $C_{mel}$  and DOPU values can be observed:  $C_{mel} = \exp[(DOPU + A)/B]$ , where  $A = -0.1408$  and  $B = -0.144$  were found by logarithmic fitting of the experimental data ( $R^2 = 0.984$ ). These results suggest that there may be a connection between the polarization scrambling observed in the human RPE and the melanin granules contained in the RPE cells.

The polarization state of light backscattered from tissue depends on the size, shape, refractive index, and concentration of the scattering particles as well on the polarization state of incident light [40–42]. While already single scattering events can modify the polarization state of backscattered light, the effective, accumulated polarization state after multiple scattering events may be random, i.e. depolarized. In order to illustrate the effect of multiple scattering events on the PS-OCT signal, a standard sample was used [40,42,43]. In exact analogy to the experiments with the melanin phantoms described above, suspensions of polystyrene spheres (Sigma Aldrich) with 1.1  $\mu\text{m}$  mean particle size were investigated. PS-OCT measurements were performed at different latex bead concentrations. The results shown in Fig. 7 reveal a similar dependence of depolarization on the particle concentration: On one hand, severe depolarization manifests as a plateau for higher concentrations of polystyrene spheres. For lower microparticle concentrations, on the other hand, an increase of DOPU values can be observed. Note, however, that the DOPU at the plateau settles at a slightly higher value. Also, the break of slope (between the logarithmic decrease and the plateau) occurs at a lower volume concentration. These differences between the depolarization characteristics of the polystyrene and melanin samples may be attributed to differences in shape and optical properties. However, the overall similarity of the PS-OCT measurements in the suspensions of latex beads to those in melanin granules indicates the similar relationship between scattering and depolarization. Further in-depth investigations of depolarization and its dependence on particle shape, size and concentration are to be exploited in future PS-OCT studies.

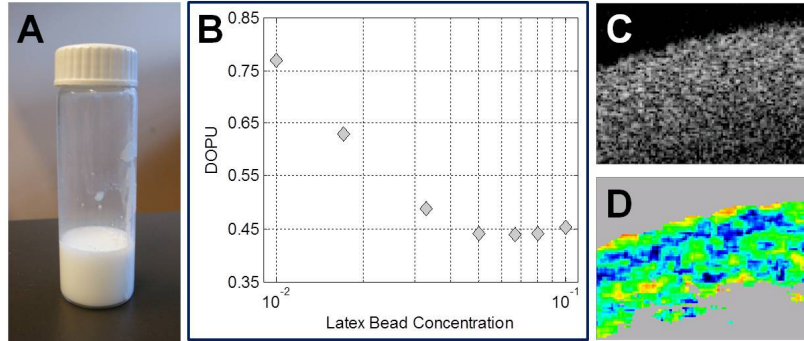


Fig. 7. PS-OCT measurements of suspensions containing polystyrene microparticles with a mean diameter of 1.1  $\mu\text{m}$ . (A) Latex bead suspension. (B) DOPU vs. latex bead concentration. For microparticle suspensions with volume concentrations ranging from 1:100 to 1:10, average DOPU values measured within the suspensions are plotted. A trend from high to low DOPU values can be observed when the concentration is increasing. (C, D) Reflectivity and DOPU B-scan images for a latex bead concentration of 1:20. See Fig. 3 for color bar of (D). Image size: 1.00 (x)  $\times$  0.25 (z)  $\text{mm}^2$ .

Retinal PS-OCT imaging in normal subjects yields a repeatable pattern with high DOPU values (i.e., no depolarization) in the neural retina and low DOPU values (i.e., strong depolarization) in the RPE (cf. e.g [14,26], and Figs. 1 and 4). In subjects with RPE disorders, such as patients suffering from late-stage non-exudative AMD (geographic atrophy), the depolarizing layer vanishes wherever the RPE cells are gone [19,24,25]. In contrast, highly pigmented choroidal naevi appear as polarization scrambling structures [44]. Here, we are filling the missing link between the complete lack of RPE cells and the presence of unusual ocular pigmentation by investigating PS-OCT images of albino patients. The effect of irregular pigmentation of the RPE cells can be observed as a reduction or as a complete lack of polarization scrambling in the RPE in Figs. 5 and 6, respectively.

Albinism is an inherited disorder of melanin biosynthesis [45]. Structural abnormalities resulting from the disrupted normal retinal development, such as foveal hypoplasia as one of the more commonly associated ocular phenotypes, have been investigated using standard spectral domain OCT [46,47]. While the absent or reduced melanin pigment in the fundi was not imaged with polarization contrast in those studies, a similar appearance of the RPE in the fovea centralis – two tightly spaced thin layers rather than one diffuse layer at the level of the RPE (cf. Figs. 4–6) – was observed [47]. It is remarkable that similar features of the RPE/BM complex were observed in the periphery of the macula in normal subjects using ultrahigh resolution OCT [48,49]. The structural differences between normals and albino patients may be connected to a lower level of highly scattering melanin pigment where the RPE/BM complex appears less fuzzy. The fuzzy appearance may be explained by multiple scattering of light by the melanin granules. Multiple scattering effects could also be responsible for the thickened, smeared out appearance of the RPE, which is actually a single cell layer with reported thicknesses of only 10-16  $\mu\text{m}$  in the macular region [28,32,50]. Furthermore, multiple scattering or scattering at particles with dimensions close to the wavelength are possible causes of the light's polarization changes that can be observed as polarization scrambling. Just like the previously discussed reduction of polarization scrambling in the peripheral RPE, the structural observations are also in agreement with the fact that the normal melanin pigmentation has a maximum in the fovea centralis (cf. Fig. 1(H)).

Our PS-OCT results agree well with earlier reports using other techniques: Ultrastructural investigations of macular pigmentation have shown that there is an inverse relationship between RPE lipofuscin concentration and RPE melanin concentration [51]: While RPE melanin has a maximum in the fovea centralis, the amount of RPE lipofuscin has a consistent dip there [28]. Furthermore, it was found in an animal study that near-infrared autofluorescence associated with RPE melanin was observable in a pigmented rat retina and almost not visible in the albino rat retina [52]. This result was in agreement with the lack of

photoacoustic signals linked to RPE melanin in albino rat retinas, while the RPE was well visible in pigmented rats [53]. In contrast, lipofuscin autofluorescence was observed in the RPE of both pigmented and albino rats [52,53]. Similar findings were reported in a histopathological study of human oculocutaneous albinism [54]. All of these results are in excellent agreement with the results from PS-OCT imaging presented in this paper and underscore the thesis that polarization scrambling observed in the RPE is connected to the melanin contained in these cells.

Using ultrastructural morphometry, Feeney-Burns et al. found that on average, 3.5 – 8% of a human RPE cell is occupied by melanin granules [27]. From our phantom measurements (Fig. 3), average DOPU values between 0.49 and 0.61 would be expected for  $C_{\text{mel}} = 0.035$  to 0.08. These numbers are in good agreement with the actual DOPU values observed in the normal retinas (green to blue mapping in Figs. 1(B), 1(D) and 4(C)) as well as with our recently reported investigation of the macular depolarization patterns in the human RPE [26]. There, mean DOPU values between 0.39 and 0.60 were measured in the central and peripheral regions of the macula, respectively. This consistence between the morphometric investigations of the RPE anatomy and the depolarization measurements indicate that PS-OCT could enable in vivo quantification of melanin concentration in the RPE and possibly other pigmented structures.

The results presented in this study are the first PS-OCT imaging results in the human retina in albinism. Only very recently, PS-OCT was performed for the first time in the retina of pigmented and albino rats [55]. In good agreement with the PS-OCT images in humans presented here, the retina in albino rats lacked polarization scrambling structures, whereas strong depolarization was observed in the highly melanin pigmented RPE and choroid. Polarization scrambling in the human choroid has not yet been investigated in detail, and also a more in-depth study of PS-OCT in human albino patients could help to shed some more light on the relationship of (ocular) pigmentation and polarization sensitive imaging. So far, PS-OCT imaging has just been used to segment depolarizing structures like the RPE in a binary fashion. Using quantitative depolarization data such as the DOPU, it may be possible to assess pigmentation irregularities (for instance, mild RPE depigmentation in early stage dry AMD) not only with high sensitivity but also in 3D and in real-time.

Having such a diagnostic tool for 3D quantification of melanin would not only have great impact on retinal diagnostics but could also be of great value for assessment of pathology and tissue health of other pigmented structures. With PS-OCT, polarization scrambling was also detected in the iris pigment epithelium and in the human skin [23,56]. Compared to other techniques used for pigment specific imaging such as (auto)fluorescence imaging, PS-OCT enables depth-resolved imaging rather than integrating signals from all depths for one transverse position. Recently, photoacoustic microscopy (PAM) was demonstrated for depth-resolved imaging of melanin in the human eye [53,57]. PAM is a novel imaging technique based on the spatially resolved detection of optical absorption. However, unlike for OCT, expensive short pulse light sources are required for PAM. In contrast to PAM, PS-OCT could serve as a single modality capable of both micrometer scale resolution structural imaging and tissue-specific mapping in 3D.

## 5. Conclusion

In this study, we investigated the polarization properties of melanin with PS-OCT. Melanin phantoms were prepared from ovoid melanin particles suspended in water at different concentrations. PS-OCT images of these suspensions revealed a correlation between the phantoms' polarization scrambling characteristics and the melanin concentration. Depolarization (manifesting in low DOPU values) was more pronounced for higher concentrations of melanin, and decreased for lower melanin concentrations. The polarization scrambling character of the melanin suspensions was in analogy to that of pigmented ocular structures like the RPE, which contain melanin granules of similar size and shape. Therefore, it is likely that the depolarizing appearance of the pigment epithelia of iris and retina be caused by the melanin granules contained within. Retinal PS-OCT imaging in albino patients

and subjects with normal pigmentation revealed pronounced polarization scrambling in the normal RPE, while less or even absent depolarization was observed in the albinos' RPE. These results suggest that PS-OCT might be a powerful technique for 3D imaging of pigmented structures.

### **Acknowledgments**

The authors thank Christoph Wölfl at Medical University of Vienna as well as David Stifter and Martin Wurm at Recendt GmbH for their outstanding technical support. Fruitful discussions with Chao Zhou, WooJhon Choi, and James G. Fujimoto at Massachusetts Institute of Technology are gratefully acknowledged. Financial support from the European Union (project FUN OCT, FP7 HEALTH, contract no. 201880) and from the Austrian Science Fund (FWF grant P19624-B02) is gratefully acknowledged.